ACS ES&T Engineering

pubs.acs.org/estengg

Article

Plasmon-enhanced Catalytic Ozonation for Efficient Removal of Recalcitrant Water Pollutants

Wenwen Yang, Muntaseer Bunian, Xiankun Chen, Steve Heald, Lei Yu, Jianguo Wen, Yu Lei,* and Tingting Wu*

Cite This: *ACS EST Engg.* 2021, 1, 874−883

Read Online

ACCESS | Metrics & More | Article Recommendations | Supporting Information

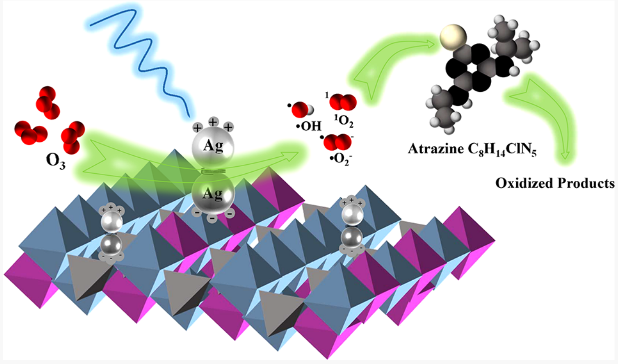

ABSTRACT: Ag-Doped $MnFe_2O_4$ catalyst ($Ag/MnFe_2O_4$) was synthesized by a simple sol−gel method followed by H_2 reduction. Utilizing the localized surface plasmon resonance (LSPR) of Ag, ~35-fold and ~7-fold degradation rate increases for a representative ozone-resistant water pollutant (atrazine) were achieved with a low photon flux (~10^{-10} Einstein L^{-1}), as compared to ozonation and catalytic ozonation, respectively, which also outperformed the homogeneous peroxone (O_3/H_2O_2) process. The plasmon-mediated enhancement was realized through energy transferred from plasmonic Ag nanostructures to ozone adsorptive sites during the LSPR decay, leading to an accelerated ozone decomposition and subsequent radical generation (e.g., ·OH, $O_2·^-$, and $^1O_2$) at both existing and newly activated catalytic active sites. Ag LSPR also helps maintain Ag^0 in an oxidizing aqueous environment, which is crucial to sustain the high catalytic activity. Because of these plasmonic effects, more than 90% removal was achieved in tap water under realistic water treatment conditions.

KEYWORDS: *Localized surface plasmon resonance (LSPR), Heterogeneous catalytic ozonation, Water pollutants, Silver, Spinel ferrite*

1. INTRODUCTION

Contamination of the aquatic environment with thousands of toxic organic compounds is a key environmental problem.[1,2] While conventional water/wastewater treatment has limited removal efficiencies for many of the recalcitrant pollutants,[3,4] advanced oxidation processes (AOPs) can permanently destroy the pollutants through an in situ generation of highly reactive species such as hydroxyl radicals (·OH) in a sufficient quantity to affect the water purification.[5,6] In particular, ozone (O_3) has long been used in water treatment, and ozone-based AOPs (e.g., O_3/H_2O_2) are reported to be more energy efficient than UV-based processes (e.g., UV/H_2O_2, UV/O_3) in terms of organic pollutants abatement.[7−9]

Ozone-based AOPs usually involve agents (e.g., H_2O_2) that can promote O_3 decomposition to initiate and propagate the formation of ·OH resulting in the faster and unselective indirect reaction pathway.[10] As the addition of H_2O_2 represents a substantial cost, especially when chemical transport/storage and destruction of excess dose are taken into account, heterogeneous processes utilizing solid catalysts appear to be an attractive option.[11−13] Metal/metal oxides are the most commonly used catalysts to promote ozone decomposition in both gaseous and aqueous phases.[14−16] The overall decomposition generally includes a dissociative adsorption of O_3 and subsequent decomposition of intermediate products or reactions of the intermediate products with O_3, during which reactive oxygen species such as ·OH can be generated. It is recommended that an effective catalyst for ozone decomposition should not only have a good reactivity with ozone (e.g., adsorption and decomposition ability) but also have "appropriately strong" bonds with the oxygen species formed during ozone decomposition. In other words, if the oxygen species on a catalyst surface are very stable, the desorption of these species becomes the rate-limiting step and impedes the overall ozone decomposition. Moreover, for aqueous ozonation reactions, the stability of the catalysts in the strong oxidizing environment can also be a concern, which may lead to catalyst deactivation as well as a degradation of the treated water quality.[17−19]

Plasmonic metal nanostructures (e.g., Au, Ag, and Cu) can interact strongly with electromagnetic radiation such as photons through an excitation of localized surface plasmon resonance (LSPR) when the frequency of photons matches the

Received: January 13, 2021
Revised: March 2, 2021
Accepted: March 15, 2021
Published: March 23, 2021

natural oscillation frequency of the surface electrons. LSPR can build up intense oscillating electric fields in the neighborhood of the nanostructure that are several orders of magnitude higher than that of the incoming photon flux,[20−22] through which plasmonic nanostructures may channel the energy of photons of Sun-like intensities to drive chemical transformations.[23−25] As Ag/Ag oxides have long been used as ozone decomposition catalysts; it is possible that an even lower photon energy input can result in a noticeable enhancement of the reaction rate, since ozone decomposition is a thermodynamically favorable process ($\Delta G^0_{298} = -163$ kJ/mol, $\Delta H^0_{298} = -138$ kJ/mol) with low activation energy using proper catalysts.[26]

Herein, we report the first study on plasmon-enhanced catalytic ozonation for the degradation of recalcitrant water pollutants. Atrazine (ATZ), a widely used herbicide, was selected as a model ozone-resistant pollutant ($k_{O3,\ pH=7} = 6$ $M^{-1}\cdot s^{-1}$, $k_{\cdot OH} = 3.0 \times 10^9$ $M^{-1}\cdot s^{-1}$).[27] H_2-reduced Ag-doped spinel ferrite (Ag/$MnFe_2O_4$) was prepared and used as the catalyst. We chose spinel ferrite as the substrate for plasmonic nanostructures because the stable mineralogical structure can prevent metallic ion leaching, and also because the enriched surface hydroxyl groups can provide active sites for catalytic ozone decomposition, as reported in previous studies.[28,29] Monochromatic blue light-emitting diode (LED, 470 ± 10 nm) was employed as a low-energy light source. The main objective of this paper was to demonstrate that, with a low photon input (~10^{-10} Einstein $L^{-1}\cdot s^{-1}$), the ATZ degradation rate can be dramatically increased compared to ozonation and catalytic ozonation, owing to the plasmonic effects of Ag. A further research effort was taken to investigate the underlying mechanism of such plasmon-mediated enhancement and possible ozone decomposition pathways. Lastly, the performance of plasmon-enhanced catalytic ozonation for ATZ removal was evaluated in tap water.

2. EXPERIMENTAL SECTION

2.1. Chemicals and Reagents. All chemicals were of analytical grade and were used as received without further purification. The detailed information on chemicals and reagents is provided in the Supporting Information (Text S1).

2.2. Catalyst Synthesis. Spinel ferrites ($MnFe_2O_4$) were synthesized using a one-pot sol−gel autocombustion method as detailed in Text S1. Ag-doped $MnFe_2O_4$ was prepared following the same procedure except that a certain amount of Ag (NO_3) (0.25−1 wt % Ag relative to Mn) was added into the precursor solution along with manganese and ferric salts.

2.3. Characterization. X-ray diffraction (XRD) patterns were collected on a Rigaku MiniFlex 600. Transmission electron microscopy (TEM), high-resolution transmission electron microscopy (HR-TEM), and selected area electron diffraction (SAED) characterizations were conducted using Argonne chromatic aberration-corrected TEM (ACAT; FEI Titan 80-300 ST with an image aberration corrector) at an accelerating voltage of 200 kV. X-ray absorption spectroscopy (XAS) measurements including X-ray absorption near edge structure (XANES) and extended X-ray absorption fine structure (EXAFS) were conducted for Ag K (~25 514 eV), Fe K (~7112 eV), and Mn K (~6539 eV) edges at beamline 20-BM at the Advanced Photon Source at Argonne National Laboratory using a double crystal Si(111) monochromator. The XAS spectra were recorded in the fluorescence mode for Ag K edge and in the transmission mode for Mn K and Fe K edges. The samples were pressed into pellets and protected with kapton tape. X-ray photoelectron spectroscopy (XPS) was examined using Thermo Scientific ESCALAB 250Xi. The specific surface area was measured with the Brunauer-Emmett-Teller (BET) method on a Quantachrome Autosorb IQ-MP/XR at 77K (Table S1).

2.4. Catalytic Ozonation Experiments. Catalytic ozonation experiments were conducted in a batch reactor illuminated externally by two LEDs (470 ± 10 nm) (Figure S2). The ozone solution was first prepared in a 1 L Erlenmeyer flask by continuously feeding ozone gas into the container, where ozone was generated by an ozone generator (MP5000, A2Z Ozone Inc.) with pure oxygen as the feeding gas. To start an experiment, catalysts, atrazine, and 150 mL of ozone solution were added into the reactor, and the mixture was continuously stirred at 500 rpm at room temperature (22 ± 2 °C). Unless otherwise noted, experiments were conducted in unbuffered deionized (DI) water to eliminate the interfering effects of other inorganic ions.[30] The initial pH was adjusted to a desired value using NaOH, and the pH evolution during the experiments was monitored. Samples were taken at predetermined time intervals, quenched by $Na_2S_2O_3$ to remove the residual ozone, and then filtered through a 0.45 μm filter for a further analysis. Addition of $Na_2S_2O_3$ and filtration had no effects on the ATZ quantification (data not shown). All experiments were conducted at least in duplicate, and the error bars in the figures indicate standard deviations. Concentrations of atrazine were measured by high-performance liquid chromatography (HPLC, Agilent 1100 series) and HPLC/MS/MS (DionEX UltiMate 3000-LTQ Orbitrap XL). Electron paramagnetic resonance (EPR) spectra were collected on a Bruker Elexsys1 × 10^{-10} E580 series X-band Fourier transform (FT) EPR at room temperature. Detailed information regarding analytical analysis of atrazine and dissolved ozone (DO_3) and determination of the photon flux is provided in the Supporting Information (Text S1).

3. RESULTS AND DISCUSSION

3.1. Catalyst Characterization. The crystalline phases of $MnFe_2O_4$ with and without Ag doping were explored by XRD patterns (Figure 1A), which agree well with the standard JCPDS (Card No. 10-0319) for the magnetic spinel $MnFe_2O_4$,[31] suggesting that Ag doping did not change the spinel structure. While $MnFe_2O_4$ calcined in air ($MnFe_2O_4$_air) and $MnFe_2O_4$ calcined in H_2 ($MnFe_2O_4$) exhibited the same diffraction peaks, the Bragg's angle of the (311) peak of 0.5 wt % Ag/$MnFe_2O_4$_air slightly shifted toward lower 2θ values by 0.30° (Figure 1B), indicating an increase in the lattice parameter values (Text S2 and Table S2). This may result from the substitution of Mn^{2+} with a smaller ionic radius (0.7 Å) by Ag^+ with a lager ionic radius (1.15 Å). In other words, Ag^+ ions have infiltrated into the lattice of $MnFe_2O_4$ and generated stress in the crystal lattice.[32] When Ag-doped $MnFe_2O_4$ was calcined in H_2 (0.5 wt % Ag/$MnFe_2O_4$), the diffraction peak of (311) shifted toward a lower 2θ further (Figure 1B). This can be ascribed to the generation of oxygen vacancies during the H_2 treatment (which is compensated for by the valence change of Ag ions ($Ag^+ \rightarrow Ag^0$) or is occupied by a hydrogen atom).[33] Hence, the Ag exsolution might have occurred.[34] High-resolution transmission electron microscopy (HRTEM) images of 0.5 wt % Ag/$MnFe_2O_4$ taken in the [100], [112], and [111] zone axes are shown in Figure 1C−F. The lattice fringes calculated from

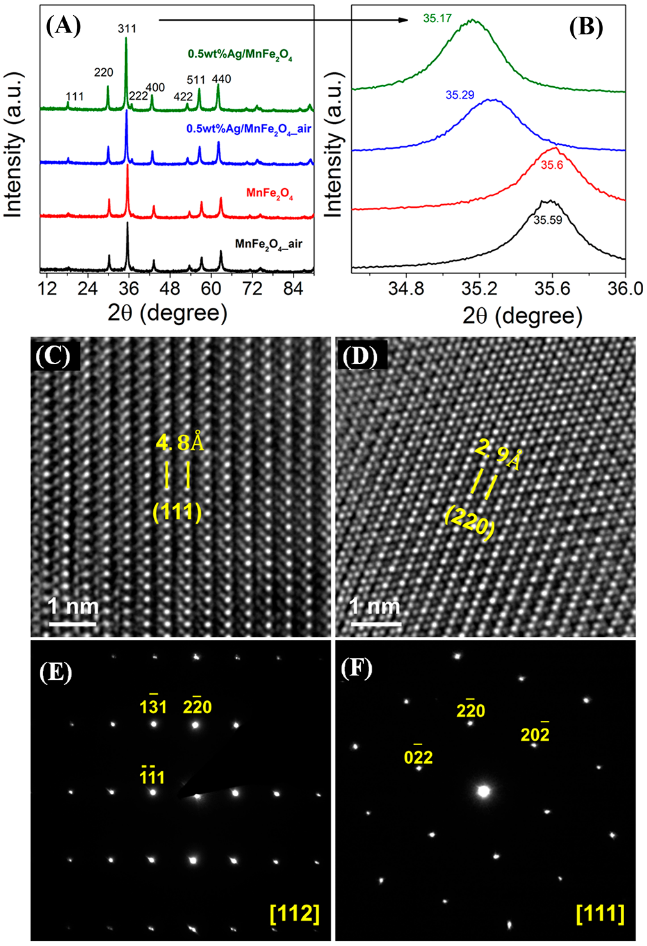

Figure 1. XRD patterns of catalysts with and without Ag doping (A, B) [A: continuous model, step size = 0.01 degree, speed = 0.5 degree/min; B: step scan mode: step size = 0.01 degree, count time = 5 s]; HRTEM images of 0.5%Ag/MnFe$_2$O$_4$ (C−F) [C: (111) lattice fringe; D: (220) lattice fringe; E: SAED pattern along [112] zone axes; and F: SAED pattern along [111] zone axes.

both HRTEM and SAED agree well with those obtained from XRD results (Table 1), which are also similar to that of MnFe$_2$O$_4$ except for a contraction of (220) and (311) planes. This could be an indication of the crystal structure being altered by the addition of Ag. The oxidation state of the metal species in 0.5 wt % Ag/MnFe$_2$O$_4$ was probed by XANES measurements. As shown in the normalized spectra of K-edge XANES (Figure 2), the oxidation state of Fe in both MnFe$_2$O$_4$ and 0.5 wt % Ag/MnFe$_2$O$_4$ is comparable to that of Fe$_3$O$_4$ (Figure 2B). The Mn K edge spectra of 0.5 wt % Ag/MnFe$_2$O$_4$ are similar to that of Mn$_3$O$_4$, which has a mean valence of 2.67. In addition, the broadening pre-edge peaks shown in Figure 2D suggest that the predominant manganese is in the octahedral sites, since a tetrahedral site occupancy leads to a sharper pre-edge peak.[35] On the basis of a linear combination fitting (LCF) of Ag K edge XANES spectra, Ag^0 and Ag$^+$ account for 22% and 78% of Ag in the bulk catalyst, respectively. The majority Ag$^+$ can be assigned to the Ag$^+$ incorporated in the manganese ferrite structure, while the rest comes from the oxidized surface of silver (Ag^0) nanoparticles under ambient conditions. The XANES results also agree well with the XPS spectra (Figure S3; Text S3). Further, an EXAFS fitting was performed to obtain quantitative information on the inversion degree of the spinel manganese ferrite, and a general formula $[Mn_{0.22}Fe_{0.78}]^A[Mn_{0.78}Fe_{1.22}]^BO_4$ was derived, where A and B represent the tetrahedral and octahedral sites, respectively. A detailed analysis and discussion is provided in Text S4, Tables S3−S5, and Figures S4 and S5.

Table 1. Comparison of Measured Lattice Spacing along Respective (hkl) Indexes of 0.5%Ag/MnFe$_2$O$_4$ and Standard MnFe$_2$O$_4$ Lattice Spacing

		lattice fringe (Å)			
(hkl)	2θ	XRD	HRTEM	SAED	standard
(111)	18.15	4.87	4.8	4.87	4.86[66]
(220)	29.84	2.9	2.9	2.9	3.01[67]
(311)	35.17	2.54		2.54	2.56[67]

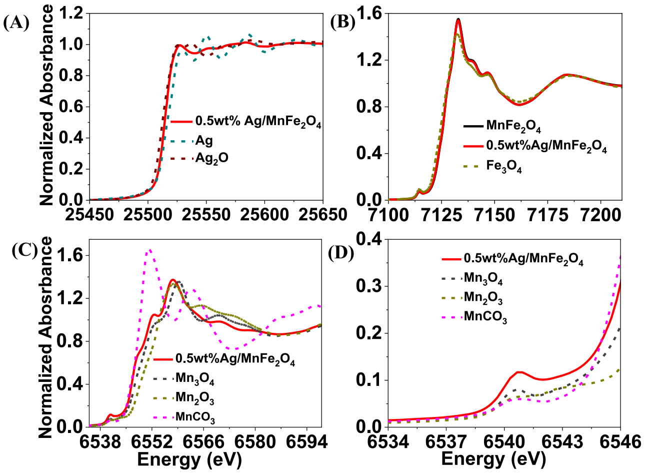

Figure 2. XANES spectra of 0.5 wt %Ag/MnFe$_2$O$_4$ with respective reference spectra at (A) Ag−K, (B) Fe−K, and (C, D) Mn−K edges.

3.2. Plasmon-Enhanced Catalytic Ozonation of Atrazine. Results of ATZ degradation under different conditions are shown in Figure 3A. Adsorption, photolysis, and photocatalysis exhibited limited removal efficiency (<10%). While single ozonation and photo-ozonation achieved 25−35% reduction in 10 min, ∼60% of the ATZ was degraded with 0.5 wt % Ag/MnFe$_2$O$_4$ as the ozonation catalyst. However, ∼65% of the ATZ was eliminated within 1 min, and a total removal greater than 95% was realized in 15 min with the addition of light irradiation (470 nm). The faster ATZ degradation also corresponded to a faster ozone depletion (Figure S6), indicating the important role of efficient ozone decomposition. Various amounts (20−30 μg/L) of metal ions (i.e., Ag, Fe, or Mn) were detected at the end of experiments, which showed no effect on ATZ removal in the presence of ozone with or without light (data not shown). This confirms the heterogeneous catalytic pathway as well as the stable mineralogical structure of Ag/MnFe$_2$O$_4$.[17] While many radical chain reactions may be involved, the overall decay of ATZ followed a simple second-order kinetics with a rate constant K_{ATZ} of 0.091 and 0.636 (mg/L)$^{-1}$·min^{-1} for catalytic ozonation and plasmon-enhanced catalytic ozonation, respectively, that is, light irradiation led to a sevenfold enhancement (Figure 3B). More notably, this degradation rate was approximately twice as fast as that of conventional O$_3$/H$_2$O$_2$, a homogeneous process, at the same ozone dose ($[H_2O_2]_0$ = 1 mg/L). Furthermore, the light-induced enhancement exhibited

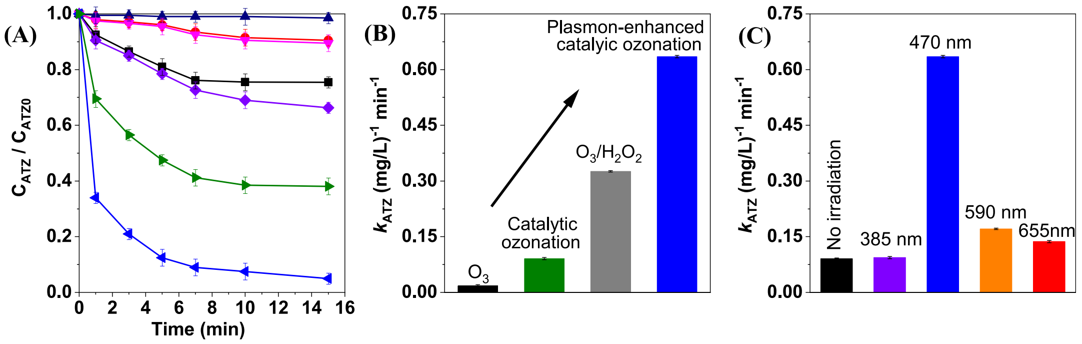

Figure 3. ATZ degradation under different conditions (A) [ozonation (black ■), photolysis (red ●; 470 nm), adsorption (black-blue ▲), photocatalysis (pink ▼), photo-ozonation (purple ◆; 470 nm), catalytic ozonation (green ▶), plasmon-enhanced catalytic ozonation (blue ◀; 470 nm)]; comparison of ATZ degradation rates (B); and effect of the irradiation wavelength (C). [Experimental conditions: Initial ATZ concentration: 2 mg/L; initial O_3 concentration (when added): 2.7 mg/L; initial H_2O_2 concentration (when added): 1 mg/L; working solution: 150 mL; catalyst dose: 1.2 g/L; light source: LEDs; photon flux (when irradiated): 6.4 × 10^{-10} Einstein $L^{-1}\cdot s^{-1}$; pH_0 = 7.].

a high wavelength dependence, with the maximum achieved at the wavelength corresponding to the Ag surface plasmon band (Figure 3C). This is a clear indication of plasmonic effects, which is also supported by the superior performance of 0.5 wt % Ag/$MnFe_2O_4$ compared with that of 0.5 wt % Ag/$MnFe_2O_4$_air under light irradiation (Figure S7). It should also be emphasized that the volumetric photon flux dosed into the solution was only 6.4 × 10^{-10} Einstein $L^{-1}\cdot s^{-1}$, which is several orders of magnitude lower than those used in photocatalytic ozonation reported in the literature (10^{-5}–10^{-8} Einstein $L^{-1}\cdot s^{-1}$).[36−38] To further put this into perspective, the solar flux is ~6 × 10^{-3} Einstein $m^{-2}\cdot s^{-1}$ with ~7.6% between 450 and 500 nm.[39] This means that, without considering other interferences and limitations of environmental matrices, the intensity of the sunlight impinging on 1 m^2 of earth may drive the catalytic ozone decomposition mediated by Ag LSPR for the treatment of >100 m^3 water, demonstrating the great potential of a plasmon-enhanced catalytic ozonation as an energy-efficient AOP for water purification. The pH evolution during the experiments was shown in Figure S8. All pH profiles exhibited a similar trend, where it quickly increased within ~1 min due to atrazine degradation (e.g., dealkylation) and then remained at a relatively constant value throughout the run, with the final pH varied between 7.7 and 7.9. Such a narrow pH range also confirms that the observed performance enhancement was not caused by a significant pH difference between different processes.

The effects of operating variables (e.g., pH, ozone/catalyst dose) were also examined, and the results are presented in Figures S9. Generally a higher pH favored ozone decomposition for ·OH generation, leading to a faster ATZ degradation. However, no appreciable difference was observed for pH 7 and 9. This may be explained by the fact that 0.5 wt % Ag$MnFe_2O_4$ prepared in our study has a pH_{pzc} of 6.98 (Table S1). Catalysts usually have the maximum ozone decomposition capability when surface hydroxyl groups are mostly zero-charged,[14,30,40] and consequently the ATZ removal efficiency was increased. As the main reactive oxidant, a higher O_3 dose led to a faster ATZ removal (Figure S9B). Similarly, a higher catalyst dose can provide more actives sites, thus enhancing the ozone decomposition and ATZ removal (Figure S9C). However, a further increase of the catalyst dose from 1.2 to 1.5 g/L resulted in no improvement in the ATZ removal, indicating the O_3 dose could be the limiting factor under the experimental conditions here. We also identified and quantified the transformation products of ATZ during the different treatment. Details can be found in the Supporting Information (Text S5, Figures S10 and S11).

3.3. Reactive Sites and Mechanism of Plasmon-Mediated Enhancement. To gain a deeper understanding of the plasmon-mediated enhancement in catalytic ozonation, we first tested $MnFe_2O_4$ as a control catalyst, where very limited catalytic activity was observed with or without light irradiation (Figure S12). These results indicate the important role of Ag/Ag_2O. For metal-based heterogeneous catalysts, surface hydroxyl groups (−OH) and/or metal redox sites (often covered by −OH in aqueous solutions) are usually the catalytic active sites for ozone decomposition.[41] Here the resulting inhibition on AZT removal upon addition of phosphate as a strong Lewis base to substitute the surface −OH supports such statement (Figure S13). Moreover, structural defects such as oxygen vacancies are reported to be the active sites in catalytic ozonation.[42,43] To further probe the possible catalytic reactive sites, we conducted XPS analysis on both pristine and used catalysts. For O 1s spectra, the peak area ratio of P_1 (lattice oxygen) to P_2 (−OH and other surface-adsorbed O) is often used to reflect the relative abundance of different oxygen species.[44,45] As shown in Figure 4A, the P_1/P_2 ratio is lower for $MnFe_2O_4$ than for the Ag-doped one, indicating the abundant −OH and surface-adsorbed O in the spinel substrate (but apparently not "energetic" enough to induce an efficient O_3 decomposition). After reactions, the P_1/P_2 of 0.5 wt % Ag/$MnFe_2O_4$ decreased, meaning the consumption of lattice oxygen and/or formation of −OH or other chemisorbed oxygen. Valence changes occurred to all the metal species after reactions indicating their active involvement in the catalytic process (Figure 4B−D). In particular, the distribution of Ag and Mn species is clearly influenced by light irradiation and further trends with the photon flux, implying the associated reactive sites are more photoresponsive. Besides being active sites for the dissociative ozone adsorption, Ag/Ag_2O are characterized by the excellent mobility of charge carriers and can facilitate an efficient electron shuttling at the nearby redox sites (e.g., Mn^{2+}/Mn^{3+}).[28,46]

Under light irradiation at the surface plasmon band of Ag, the Ag nanoparticle acts as a nanoconcentrator through LSPR that concentrates and amplifies the incoming photon flux in small volumes surrounding the nanostructure.[24,47,48] The decay of LSPR can lead to energy transfer from the plasmonic

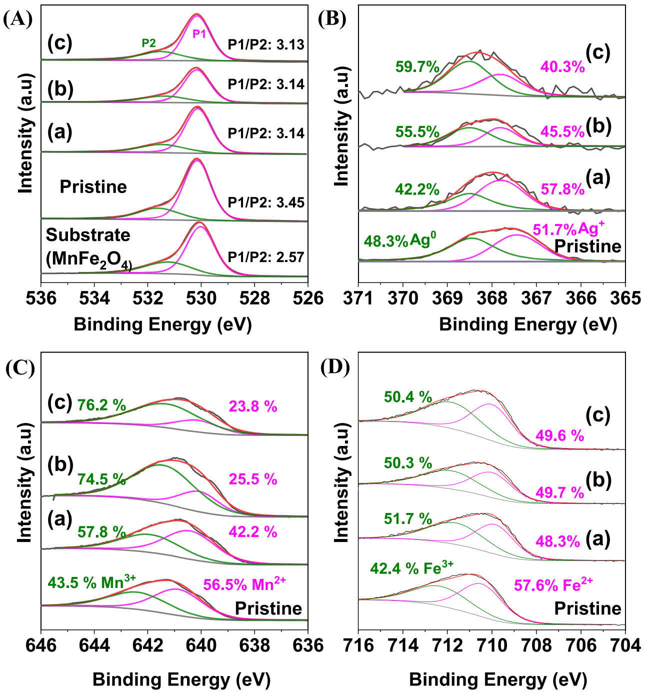

Figure 4. O 1s (A), Ag 3d (B), Mn 2p (C), and Fe 2p (D) XPS spectra of pristine and spent catalysts (0.5 wt % $Ag/MnFe_2O_4$) [(a) after catalytic ozonation; (b&c) after plasmon-enhanced catalytic ozonation, photon flux: (b) 4.28×10^{-10} Einstein $L^{-1} \cdot s^{-1}$, (c) 6.4×10^{-10} Einstein $L^{-1} \cdot s^{-1}$].

nanostructure to its surrounding environment or to local heating of the nanostructure, both of which may accelerate chemical reactions.[49] It has been suggested that, for plasmon-induced heating to have a meaningful change in reaction rates, usually a very high light intensity (orders of magnitude higher than the solar flux) or an extreme thermal isolation of the nanostructure from the environment is needed.[49−51] Here we monitored the bulk solution temperature during the experiment, and no appreciable increase was observed (Figure S14). Given the facts of the low photon flux, the continuous mixing of the working solution with the catalysts under ambient conditions, and the steady bulk temperature, the extent and consequent effects of local heating (if any) should be very limited. On the other hand, we noticed that the rate constants of ozone decomposition as well as those of ATZ degradation changed proportionally to the photon flux (Figure 5). This linear dependence is an experimental signature of charge carrier-induced chemical reactions, and other mechanisms such as heating do not exhibit this behavior.[24] All these provide compelling evidence that catalytic ozone decomposition was promoted mainly through the energy transfer from and not the equilibrium heating of the Ag particles.

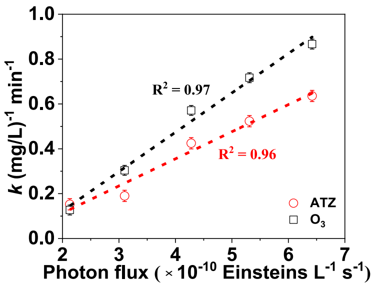

Figure 5. Reaction rate constants vs photon flux. [Experimental conditions: initial ATZ concentration: 2 mg/L; initial O_3 concentration: 2.7 mg/L; working solution: 150 mL; catalyst dose: 1.2 g/L; light source: LEDs; $pH_0 = 7$].

For the catalysts used in this study, Ag nanoparticles are in direct contact with the spinel ferrite substrate. Therefore, the incoming photon energy concentrated through Ag LSPR can be transferred to the surroundings via both radiative (e.g., electromagnetic filed) and nonradiative (e.g., formation of energetic electrons) processes.[47] The energy-transfer mechanisms by which Ag LSPR can enhance the catalytic ozone decomposition are illustrated in Scheme S1. First, Ag/Ag_2O can serve as the reactive sites for ozone decomposition. Upon an excitation of LSPR, energetic electrons can be transferred to the surface-adsorbed ozone indirectly, where energetic electrons first form on the surface of Ag nanoparticles and subsequently transfer to the adsorbate (O_3) acceptor states or through a direct plasmon-mediated charge scattering via the adsorbate,[47,49] resulting in an enhanced ozone decomposition. Under the influence of large electric fields, the electron shuttling between Ag/Ag_2O and nearby redox sites becomes much more efficient as well. Here the presence of photoejected electrons is supported by the results of electron-trapping tests with methyl viologen (MV^{2+}) (Text S6; Figure S15).[52,53] The formation of $MV^{\cdot +}$ cations was only observed under light irradiation at 470 nm, which further confirms Ag plasmonic effects. Since photocatalysis only led to very limited ATZ removal (Figure 2A), these photoejected electrons should mostly be involved in the electron-assisted ozone decomposition process directly or indirectly, during which other reactive species responsible for ATZ degradation were generated (identification of the reactive species is discussed in Section 3.4).

In addition to the enhanced catalytic activity at sites that are active even without light irradiation, we think the elevated electric fields established through LSPR may also "activate" more ozone-adsorptive sites, which are otherwise not energetic enough to overcome the activation barriers. These sites may locate at regions of proximity of the excited plasmonic nanostructure or hot spots between Ag particles (where multiple resonances exist, yielding very strong electric fields),[49] and they may be energized via a near-field electromagnetic mechanism or accelerated electron tunneling processes. Evidence to support this hypothesis could be significant impacts of the ozone-adsorptive site density on the plasmon-induced enhancement. Here we compared the performance and surface −OH density of catalysts with different Ag doping, where the validity of the surface −OH density to represent the ozone adsorption capacity was first demonstrated (Text S7, Figure S16). As shown in Figure S17A, the efficiency of ATZ removal generally increased with Ag loading for catalytic ozonation. With light irradiation, a sharp increase of k_{ATZ} was observed for 0.5 wt % $Ag/MnFe_2O_4$ as compared to 0.25 wt % $Ag/MnFe_2O_4$ and 1.0 wt % $Ag/MnFe_2O_4$. In the meantime, 0.5 wt % $Ag/MnFe_2O_4$ bears the highest surface −OH density. To minimize the effects of different particle sizes and spacings caused by different Ag loadings, we also synthesized several MFe_2O_4 (M = Co, Cu, Zn, or Mn), all doped with 0.5 wt % Ag. A similar impact of surface −OH density on k_{ATZ} was observed (Figure S17B). The significance of these results is that, while multiple factors may account for the different performance of these catalysts during catalytic ozonation, a

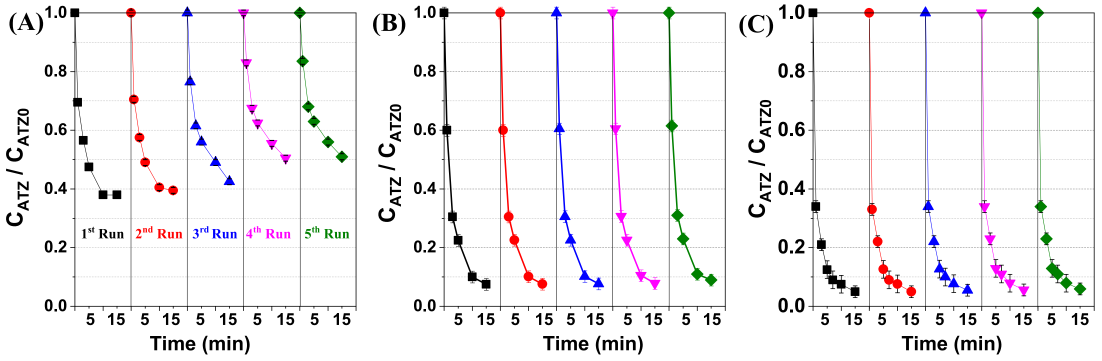

Figure 6. Cyclic runs of catalytic ozonation (A) and plasmon-enhanced catalytic ozonation (B, C). [Experimental conditions: initial ATZ concentration: 2 mg/L; initial O_3 concentration: 2.7 mg/L; working solution: 150 mL; catalyst dose: 1.2 g/L; light source: LEDs; photon flux (when irradiated): (B) 4.28 × 10^{-10} Einstein $L^{-1}\cdot s^{-1}$, (C) 6.4 × 10^{-10} Einstein $L^{-1}\cdot s^{-1}$; pH_0 = 7].

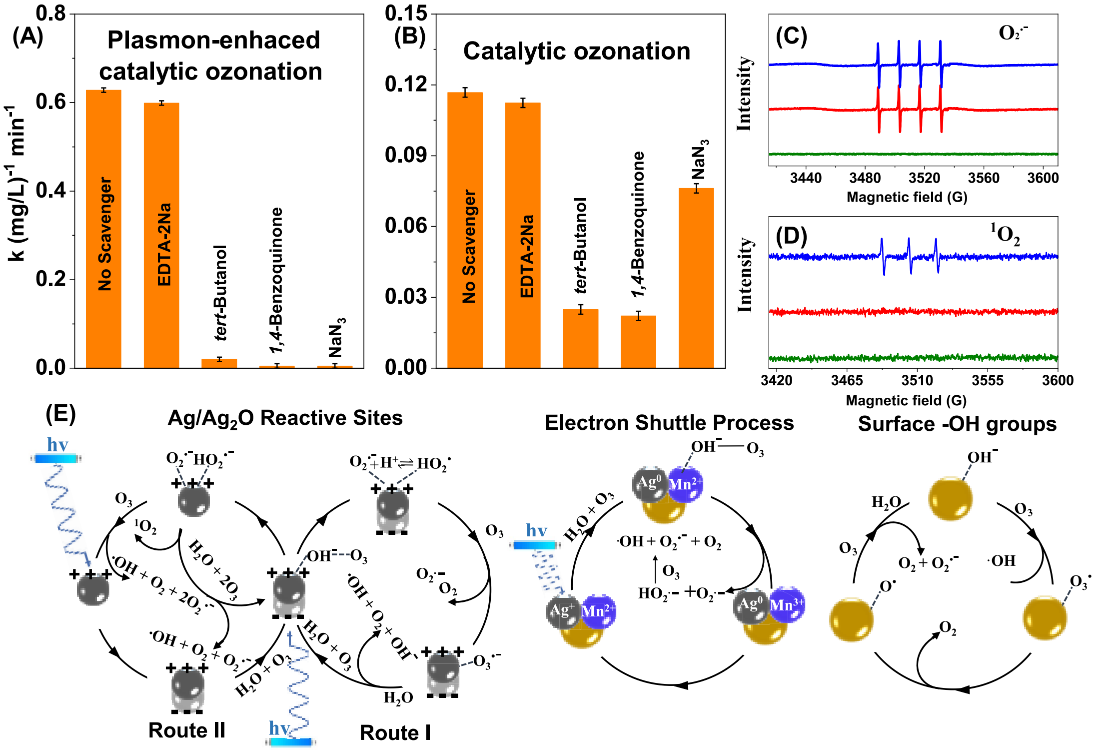

Figure 7. Effects of different scavengers on ATZ degradation (A, B) [1 mM *tert*-butanol, 1 mM EDTA-2Na, 0.370 mM 1.4-benzoquinone, 0.614 mM NaN_3]; EPR spectra of reactive oxygen species (C, D) [control (trapping agent only): green; catalytic ozonation: red; plasmon-enhanced catalytic ozonation: blue]. (E). Catalytic ozone decomposition pathways at different adsorptive sites.

much-pronounced light-mediated enhancement always occurred on the Ag-doped catalyst with the highest ozone-adsorptive sites, implying Ag LSPR may have channeled energy to and consequently activated more adsorptive sites to induce ozone decomposition. Here it is also worth mentioning that the excitation and decay of LSPR are sensitive to the composition, size, geometry, and the local environment of the plasmonic nanostructure.[48] While beyond the scope of this initial demonstration, further studies involving carefully designed and precisely synthesized nanostructures are needed to delineate these effects.

In an oxidizing aqueous environment, Ag^0 tends to be oxidized easily. However, in contrast to the decreased surface Ag^0 content after catalytic ozonation, the surface Ag^0 actually increased after the plasmon-enhanced catalytic ozonation, suggesting photoreduction of the surface Ag occurred (Figure 4B). This can be attributed to the weakening of Ag−O bonds by LSPR of the Ag core.[54] The presence of Ag^0 is crucial to sustain the high catalytic performance. As illustrated in Figure 6, 0.5 wt % Ag/$MnFe_2O_4$ exhibited excellent stability in cyclic runs, whereas the performance gradually declined during catalytic ozonation without light irradiation. Even without considering the LSPR of Ag, we believe a mixture of Ag/Ag_2O is beneficial for efficient ozone decomposition. Metal oxides have been reported to be more active toward ozone, but a decomposition that is too fast may cover the catalyst surface with stable oxygen species and therefore hinder further decomposition of ozone.[12]

3.4. Reactive Species and Possible Ozone Decomposition Pathways.

Here we conducted a series of scavenger tests and EPR measurements to investigate the reactive species that were generated and responsible for the ATZ degradation during different catalytic ozonation processes. Here, *t*-BuOH, 1,4-benzoquinone, NaN_3, and EDTA-2Na (EDTA = ethylenediaminetetraacetic acid) were employed as the scavengers for $\cdot OH$, $\cdot O_2$, $^1O_2$, and h^+, respectively.[55−57] As shown in Figure 7A,B, the effect of the EDTA-2Na addition was almost negligible, indicating h^+ was not involved in the ATZ removal. On the contrary, both *t*-BuOH and 1,4-benzoquinone inhibited ATZ degradation, implying $\cdot OH$ and $\cdot O_2$ were generated in both processes. An addition of NaN_3 affected the ATZ degradation differently during the catalytic ozonation with and without light irradiation. While a significant inhibition was observed in the plasmon-enhanced process, the effect was much less pronounced in catalytic ozonation. This implies that $^1O_2$ was mainly generated under a light irradiation. Furthermore, since 1,4-benzoquinone and NaN_3 also have strong scavenging effects against $\cdot OH$,[58,59] 5-*tert*-butoxycarbonyl-5-methyl-1-pyrroline *N*-oxide (TBMPO) and 2,2,6,6-tetramethylpiperidine (TEMP) were employed as the spin trapping agents in electron paramagnetic resonance (EPR) experiments to further probe $O_2\cdot^-$ and $^1O_2$, respectively.[60,61] The characteristic EPR signals of $TBMPO/O_2\cdot^-$ adducts (1:1:1:1 four-line spectra; Figure 7C) were detected in both processes, while the characteristic EPR signals of $TEMP/^1O_2$ adducts were only detected during the plasmon-enhanced catalytic ozonation (Figure 7D), which confirms the results of scavenger tests.

On the basis of the results and discussion above, the corresponding catalytic ozone decomposition pathways at different adsorptive sites are proposed and presented in Figure 7E. At Ag/Ag_2O sites, the intense electric field generated at the surface via LSPR excitation may lead to transient electronic excitations and consequently induce ozone decomposition, during which there is no charge extraction out of Ag (Route I).[62] Furthermore, upon plasmonic excitation, energetic charge carriers such as energized electrons can be generated and injected into the adsorbate (O_3), leading to the formation of surface-bound intermediates ($O_2\cdot$ and $HO_2\cdot$). $O_2\cdot$ can then be oxidized by the paired hole through which $^1O_2$ is released and Ag^+ returns to Ag^0 (Route II). These intermediates may also react with another ozone and be desorbed from the surface, leaving the metal nanoparticle in a charged state. As discussed previously, LSPR of the metal core can help restore the metal surface to the uncharged state. Besides, the superior electron transport properties of Ag can also facilitate the electron shuttling between Mn(II) and Mn(III) for efficient ozone decomposition,[28,46] where LSPR of the metal core helps restore the uncharged state again. Moreover, surface hydroxyl groups on the metal-based catalysts can also be the catalytic active sites for ozone decomposition and the consequent generation of hydroxyl radical ($\cdot OH$) and superoxide radical ($O_2\cdot^-$).[41,63] Note that ozone decomposition at all these adsorptive sites can be enhanced due to the plasmonic effects of Ag nanostructures. Further, as illustrated in Scheme S1, the plasmon-induced elevated field may energize more ozone-adsorptive sites and consequently enable catalytic ozone decomposition at these sites as well (discussion in Section 3.3). Future studies such as in situ Raman spectroscopy to characterize intermediate oxygen species in the presence of ozone/light should be conducted to further support the proposed pathways.[64]

3.5. Demonstration in Tap Water. Lastly, the high efficiency of plasmon-enhanced catalytic ozonation was demonstrated in tap water (Table S6) under realistic water treatment conditions. As shown in Figure 8, ~92% of ATZ removal (C_0 = 30 μg/L) was achieved in 5 min, with an O_3/TOC (total organiccCarbon)mass ratio of 0.7 and a photon flux of 4.28 × 10^{-10} Einstein $L^{-1}\cdot s^{-1}$ at 470 nm. Meanwhile, the formation of bromate, a typical ozonation byproduct, decreased from 20 μg/L for ozonation alone to 14.2 μg/L for catalytic ozonation and, further, down to 6.8 μg/L for plasmon-enhanced catalytic ozonation, which is lower than the maximum contaminant level (MCL; 10 μg/L) for drinking water set by the United States Environmental Protection Agency (USEPA).[65] For comparison, studies on heterogeneous catalytic ozonation for ATZ removal reported in the literature were summarized in Table S7. To the best of our knowledge, this is the first study that reports plasmon-enhanced catalytic ozonation can be a very efficient AOP for the elimination of recalcitrant water pollutants, which warrants further investigation. We also think spinel ferrite-based catalysts are very promising for practical applications, ascribed to its stable mineralogical structure with abundant ozone-adsorptive sites and magnetic property for easy separation, the facile and scalable synthesis route (nearly 100% yield), the superior performance of plasmon-enhanced catalytic ozonation with very low Ag loading (~0.1 wt % of the total catalyst mass) and photon input, and the good recyclability.

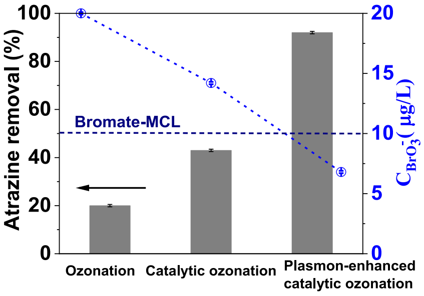

Figure 8. ATZ removal and bromate formation in tap water. [Experimental conditions: test in tap water: initial ATZ concentration: 30 μg/L, working solution: 150 mL, catalyst dose: 1.3 g/L, photon flux (when irradiated): 4.28 × 10^{-10} Einstein $L^{-1}\cdot s^{-1}$, O_3/TOC (mass ratio): 0.7, reaction time: 5 min].

4. CONCUSION

In this study, we have demonstrated for the first time that the treatment efficiency of recalcitrant organic water pollutants by heterogeneous catalytic ozonation can be significantly enhanced utilizing the LSPR of Ag on $Ag/MnFe_2O_4$ with a photon input as low as ~10^{-10} Einstein $L^{-1}\cdot s^{-1}$ at the Ag plasmon band. The high and stable catalytic activity of $Ag/MnFe_2O_4$ can be ascribed to the LSPR of Ag, which not only enables energy transfer to the ozone-adsorption site and consequently leads to the enhanced ozone decomposition and subsequent generation of reactive oxygen species (e.g., $\cdot OH$, $O_2\cdot^-$, and $^1O_2$) for organic degradation, but also helps maintain Ag^0 in the catalysts in an oxidizing aqueous environment. We think this work is of great environmental significance. It paves the way for the development of plasmon-enhanced catalytic ozonation processes for the efficient elimination of refractory organic pollutants in water treatment. It also sheds light on designing plasmonic photocatalysts for gaseous ozone decomposition for air pollution control.

■ ASSOCIATED CONTENT

Supporting Information

The Supporting Information is available free of charge at https://pubs.acs.org/doi/10.1021/acsestengg.1c00020.

Catalyst synthesis and characterization, relevant analytical methods, and catalytic performance (PDF)

■ AUTHOR INFORMATION

Corresponding Authors

Yu Lei − *Department of Chemical and Materials Engineering, The University of Alabama in Huntsville, Huntsville 35899, Alabama, United States;* orcid.org/0000-0002-4161-5568; Email: Yu.Lei@uah.edu

Tingting Wu − *Department of Civil and Environmental Engineering, The University of Alabama in Huntsville, Huntsville 35899, Alabama, United States;* orcid.org/0000-0002-4653-8493; Email: Tingting.Wu@uah.edu

Authors

Wenwen Yang − *Department of Civil and Environmental Engineering, The University of Alabama in Huntsville, Huntsville 35899, Alabama, United States*

Muntaseer Bunian − *Department of Chemical and Materials Engineering, The University of Alabama in Huntsville, Huntsville 35899, Alabama, United States*

Xiankun Chen − *Department of Civil and Environmental Engineering, The University of Alabama in Huntsville, Huntsville 35899, Alabama, United States*

Steve Heald − *X-ray Science Division, Argonne National Laboratory, Lemont 60439, Illinois, United States*

Lei Yu − *Center for Nanoscale Materials, Argonne National Laboratory, Lemont 60439, Illinois, United States*

Jianguo Wen − *Center for Nanoscale Materials, Argonne National Laboratory, Lemont 60439, Illinois, United States*

Complete contact information is available at: https://pubs.acs.org/10.1021/acsestengg.1c00020

Notes

The authors declare no competing financial interest.

■ ACKNOWLEDGMENTS

This work is financially supported by National Science Foundation, CBET-1606117. Use of the Advanced Photon Source and the Center for Nanoscale Materials, two Office of Science user facilities, was supported by the U.S. Department of Energy, Office of Science, Office of Basic Energy Sciences, under Contract No. DE-AC02-06CH11357.

■ REFERENCES

(1) Schwarzenbach, R. P.; Escher, B. I.; Fenner, K.; Hofstetter, T. B.; Johnson, C. A.; von Gunten, U.; Wehrli, B. The Challenge of Micropollutants in Aquatic Systems. *Science (Washington, DC, U. S.)* **2006**, *313* (5790), 1072−1077.

(2) Petrie, B.; Barden, R.; Kasprzyk-Hordern, B. A Review on Emerging Contaminants in Wastewaters and the Environment: Current Knowledge, Understudied Areas and Recommendations for Future Monitoring. *Water Res.* **2015**, *72* (0), 3−27.

(3) Stackelberg, P. E.; Furlong, E. T.; Meyer, M. T.; Zaugg, S. D.; Henderson, A. K.; Reissman, D. B. Persistence of Pharmaceutical Compounds and Other Organic Wastewater Contaminants in a Conventional Drinking-Water-Treatment Plant. *Sci. Total Environ.* **2004**, *329* (1−3), 99−113.

(4) Westerhoff, P.; Yoon, Y.; Snyder, S.; Wert, E. Fate of Endocrine-Disruptor, Pharmaceutical, and Personal Care Product Chemicals during Simulated Drinking Water Treatment Processes. *Environ. Sci. Technol.* **2005**, *39* (17), 6649−6663.

(5) Andreozzi, R.; Caprio, V.; Insola, A.; Marotta, R. Advanced Oxidation Processes (AOP) for Water Purification and Recovery. *Catal. Today* **1999**, *53* (1), 51−59.

(6) Klavarioti, M.; Mantzavinos, D.; Kassinos, D. Removal of Residual Pharmaceuticals from Aqueous Systems by Advanced Oxidation Processes. *Environ. Int.* **2009**, *35* (2), 402−417.

(7) Santiago-Morales, J.; Gómez, M. J.; Herrera-López, S.; Fernández-Alba, A. R.; García-Calvo, E.; Rosal, R. Energy Efficiency for the Removal of Non-Polar Pollutants during Ultraviolet Irradiation, Visible Light Photocatalysis and Ozonation of a Wastewater Effluent. *Water Res.* **2013**, *47* (15), 5546−5556.

(8) Rosenfeldt, E. J.; Linden, K. G.; Canonica, S.; von Gunten, U. Comparison of the Efficiency of ·OH Radical Formation during Ozonation and the Advanced Oxidation Processes O_3/H_2O_2 and UV/H_2O_2. *Water Res.* **2006**, *40*, 3695−3704.

(9) Glaze, W. H.; Kang, J.-W.; Chapin, D. H. The Chemistry of Water Treatment Processes Involving Ozone, Hydrogen Peroxide and Ultraviolet Radiation. *Ozone: Sci. Eng.* **1987**, *9*, 335−352.

(10) von Sonntag, C.; von Gunten, U. *Chemistry of Ozone in Water and Wastewater Treatment: From Basic Principles to Applications;* IWA Publishing, 2012. DOI: 10.2166/9781780400839.

(11) Loeb, S. K.; Alvarez, P. J. J.; Brame, J. A.; Cates, E. L.; Choi, W.; Crittenden, J.; Dionysiou, D. D.; Li, Q.; Li-Puma, G.; Quan, X.; et al. The Technology Horizon for Photocatalytic Water Treatment: Sunrise or Sunset? *Environ. Sci. Technol.* **2019**, *53* (6), 2937−2947.

(12) Lin, J.; Kawai, A.; Nakajima, T. Effective catalysts for decomposition of aqueous ozone. *Appl. Catal., B* **2002**, *39*, 157−165.

(13) Rosenfeldt, E. J.; Linden, K. G.; Canonica, S.; von Gunten, U. Comparison of the Efficiency of {radical Dot}OH Radical Formation during Ozonation and the Advanced Oxidation Processes O3/H2O2 and UV/H2O2. *Water Res.* **2006**, *40* (20), 3695−3704.

(14) Yuan, L.; Shen, J.; Yan, P.; Chen, Z. Interface Mechanisms of Catalytic Ozonation with Amorphous Iron Silicate for Removal of 4 - Chloronitrobenzene in Aqueous Solution. *Environ. Sci. Technol.* **2018**, *52*, 1429−1434.

(15) Jia, J.; Zhang, P.; Chen, L. Catalytic Decomposition of Gaseous Ozone over Manganese Dioxides with Different Crystal Structures. *Appl. Catal., B* **2016**, *189*, 210−218.

(16) Kasprzyk-Hordern, B.; Ziółek, M.; Nawrocki, J. Catalytic Ozonation and Methods of Enhancing Molecular Ozone Reactions in Water Treatment. *Appl. Catal., B* **2003**, *46* (4), 639−669.

(17) Yang, W.; Vogler, B.; Lei, Y.; Wu, T. Metallic Ion Leaching from Heterogeneous Catalysts: An Overlooked Effect in the Study of Catalytic Ozonation Processes. *Environ. Sci. Water Res. Technol.* **2017**, *3*, 1143−1151.

(18) Xiao, J.; Han, Q.; Xie, Y.; Yang, J.; Su, Q.; Chen, Y.; Cao, H. Is C3N4 Chemically Stable toward Reactive Oxygen Species in Sunlight-Driven Water Treatment? *Environ. Sci. Technol.* **2017**, *51* (22), 13380−13387.

(19) Yang, W.; Lu, Z.; Vogler, B.; Wu, T.; Lei, Y. Enhancement of Copper Catalyst Stability for Catalytic Ozonation in Water Treatment Using ALD Overcoating. *ACS Appl. Mater. Interfaces* **2018**, *10*, 43323−43326.

(20) Burda, C.; Chen, X.; Narayanan, R.; El-Sayed, M. A. Chemistry and Properties of Nanocrystals of Different Shapes. *Chem. Rev.* **2005**, *105* (4), 1025−1102.

(21) Gunnarsson, L.; Rindzevicius, T.; Prikulis, J.; Kasemo, B.; Käll, M.; Zou, S.; Schatz, G. C. Confined Plasmons in Nanofabricated Single Silver Particle Pairs: Experimental Observations of Strong Interparticle Interactions. *J. Phys. Chem. B* **2005**, *109* (3), 1079−1087.

(22) Linic, S.; Aslam, U.; Boerigter, C.; Morabito, M. Photochemical Transformations on Plasmonic Metal Nanoparticles. *Nat. Mater.* **2015**, *14*, 567−576.

(23) Chen, X.; Zhu, H. Y.; Zhao, J. C.; Zheng, Z. F.; Gao, X. P. Visible-Light-Driven Oxidation of Organic Contaminants in Air with

Gold Nanoparticle Catalysts on Oxide Supports. *Angew. Chem., Int. Ed.* **2008**, *47* (29), 5353−5356.

(24) Christopher, P.; Xin, H.; Linic, S. Visible-Light-Enhanced Catalytic Oxidation Reactions on Plasmonic Silver Nanostructures. *Nat. Chem.* **2011**, *3* (6), 467−472.

(25) Zhu, H.; Ke, X.; Yang, X.; Sarina, S.; Liu, H. Reduction of Nitroaromatic Compounds on Supported Gold Nanoparticles by Visible and Ultraviolet Light. *Angew. Chem., Int. Ed.* **2010**, *49* (50), 9657−9661.

(26) Green, D. W.; Southard, M. Z. *Perry's Chemical Engineers' Handbook*, 9th ed.; McGraw-Hill Education, 1997.

(27) Lee, Y.; Gerrity, D.; Lee, M.; Bogeat, A. E.; Salhi, E.; Gamage, S.; Trenholm, R. A.; Wert, E. C.; Snyder, S. A.; Von Gunten, U. Prediction of Micropollutant Elimination during Ozonation of Municipal Wastewater Effluents: Use of Kinetic and Water Specific Information. *Environ. Sci. Technol.* **2013**, *47*, 5872−5881.

(28) Wang, Z.; Ma, H.; Zhang, C.; Feng, J.; Pu, S.; Ren, Y.; Wang, Y. Enhanced Catalytic Ozonation Treatment of Dibutyl Phthalate Enabled by Porous Magnetic Ag-Doped Ferrospinel MnFe2O4materials: Performance and Mechanism. *Chem. Eng. J.* **2018**, *354* (July), 42−52.

(29) Kefeni, K. K.; Mamba, B. B.; Msagati, T. A. M. Application of Spinel Ferrite Nanoparticles in Water and Wastewater Treatment: A Review. *Sep. Purif. Technol.* **2017**, *188*, 399−422.

(30) Yang, W.; Wu, T. Investigation of Matrix Effects in Laboratory Studies of Catalytic Ozonation Processes. *Ind. Eng. Chem. Res.* **2019**, *58*, 3468−3477.

(31) Chen, J.; Wen, W.; Kong, L.; Tian, S.; Ding, F.; Xiong, Y. Magnetically Separable and Durable MnFe2O4 for Efficient Catalytic Ozonation of Organic Pollutants. *Ind. Eng. Chem. Res.* **2014**, *53* (15), 6297−6306.

(32) Makhdoom, A. R.; Akhtar, M. J.; Rafiq, M. A.; Hassan, M. M. Investigation of Transport Behavior in Ba Doped BiFeO 3. *Ceram. Int.* **2012**, *38* (5), 3829−3834.

(33) Kronenberger, A.; Polity, A.; Hofmann, D. M.; Meyer, B. K.; Schleife, A.; Bechstedt, F. Structural, Electrical, and Optical Properties of Hydrogen-Doped ZnO Films. *Phys. Rev. B: Condens. Matter Mater. Phys.* **2012**, *86* (1−8), 115334.

(34) Götsch, T.; Schlicker, L.; Bekheet, M. F.; Doran, A.; Grünbacher, M.; Praty, C.; Tada, M.; Matsui, H.; Ishiguro, N.; Gurlo, A.; et al. Structural Investigations of La0.6Sr0.4FeO3-:*δ* under Reducing Conditions: Kinetic and Thermodynamic Limitations for Phase Transformations and Iron Exsolution Phenomena. *RSC Adv.* **2018**, *8*, 3120−3131.

(35) Wei, C.; Feng, Z.; Scherer, G. G.; Barber, J.; Shao-Horn, Y.; Xu, Z. J. Cations in Octahedral Sites: A Descriptor for Oxygen Electrocatalysis on Transition-Metal Spinels. *Adv. Mater.* **2017**, *29* (23), 1606800.

(36) Piera, E.; Calpe, J. C.; Brillas, E.; Domènech, X.; Peral, J. 2,4-Dichlorophenoxyacetic Acid Degradation by Catalyzed Ozonation: TiO2/UVA/O3 and FE(II)/UVA/O3 Systems. *Appl. Catal., B* **2000**, *27*, 169−177.

(37) Beltrán, F. J.; Aguinaco, A.; García-Araya, J. F. Mechanism and Kinetics of Sulfamethoxazole Photocatalytic Ozonation in Water. *Water Res.* **2009**, *43*, 1359−1369.

(38) Aguinaco, A.; Beltrán, F. J.; García-Araya, J. F.; Oropesa, A. Photocatalytic Ozonation to Remove the Pharmaceutical Diclofenac from Water: Influence of Variables. *Chem. Eng. J.* **2012**, *189−190*, 275−282.

(39) Mecherikunnel, A. T.; Richmond, J. C. *NASA Technical Memorandum 82021. Spectral Distribution of Solar Radiation;* NASA, 1980; p 93.

(40) Yuan, L.; Shen, J.; Chen, Z.; Liu, Y. Pumice-Catalyzed Ozonation Degradation of p -Chloronitrobenzene in Aqueous Solution. *Appl. Catal., B* **2012**, *117−118*, 414−419.

(41) Yu, G.; Wang, Y.; Cao, H.; Zhao, H.; Xie, Y. Reactive Oxygen Species and Catalytic Active Sites in Heterogeneous Catalytic Ozonation for Water Purification. *Environ. Sci. Technol.* **2020**, *54* (10), 5931−5946.

(42) Wang, Y.; Chen, L.; Cao, H.; Chi, Z.; Chen, C.; Duan, X.; Xie, Y.; Qi, F.; Song, W.; Liu, J.; Wang, S.; et al. Role of Oxygen Vacancies and Mn Sites in Hierarchical Mn2O3/LaMnO3-Δ Perovskite Composites for Aqueous Organic Pollutants Decontamination. *Appl. Catal., B* **2019**, *245*, 546−554.

(43) Zhu, G.; Zhu, J.; Jiang, W.; Zhang, Z.; Wang, J.; Zhu, Y.; Zhang, Q. Surface Oxygen Vacancy Induced A-MnO2nanofiber for Highly Efficient Ozone Elimination. *Appl. Catal., B* **2017**, *209*, 729−737.

(44) Zhan, S.; Zhang, H.; Mi, X.; Zhao, Y.; Hu, C.; Lyu, L. Efficient Fenton-like Process for Pollutant Removal in Electron-Rich/Poor Reaction Sites Induced by Surface Oxygen Vacancy over Cobalt−Zinc Oxides. *Environ. Sci. Technol.* **2020**, *54*, 8333−8343.

(45) Zhang, H.; Li, C.; Lyu, L.; Hu, C. Surface Oxygen Vacancy Inducing Peroxymonosulfate Activation through Electron Donation of Pollutants over Cobalt-Zinc Ferrite for Water Purification. *Appl. Catal., B* **2020**, *270* (March), 118874.

(46) Li, X.; Ma, J.; He, H Tuning the Chemical State of Silver on Ag-Mn Catalysts to Enhance the Ozone Decomposition Performance. *Environ. Sci. Technol.* **2020**, *54*, 11566 DOI: 10.1021/acs.est.0c02510.

(47) Linic, S.; Christopher, P.; Ingram, D. B. Plasmonic-Metal Nanostructures for Efficient Conversion of Solar to Chemical Energy. *Nat. Publ. Gr.* **2011**, *10* (12), 911−921.

(48) Seemala, B.; Therrien, A. J.; Lou, M.; Li, K.; Finzel, J. P.; Qi, J.; Nordlander, P.; Christopher, P. Plasmon-Mediated Catalytic O2 Dissociation on Ag Nanostructures: Hot Electrons or Near Fields? *ACS Energy Lett.* **2019**, *4* (8), 1803−1809.

(49) Linic, S.; Aslam, U.; Boerigter, C.; Morabito, M. Photochemical Transformations on Plasmonic Metal Nanoparticles. *Nat. Mater.* **2015**, *14* (6), 567−576.

(50) Fasciani, C.; Alejo, C. J. B.; Grenier, M.; Netto-Ferreira, J. C.; Scaiano, J. C. High-Temperature Organic Reactions at Room Temperature Using Plasmon Excitation: Decomposition of Dicumyl Peroxide. *Org. Lett.* **2011**, *13* (2), 204−207.

(51) Adleman, J. R.; Boyd, D. A.; Goodwin, D. G.; Psaltis, D. Heterogenous Catalysis Mediated by Plasmon Heating. *Nano Lett.* **2009**, *9* (12), 4417−4423.

(52) Navalon, S.; De Miguel, M.; Martin, R.; Alvaro, M.; Garcia, H. Enhancement of the Catalytic Activity of Supported Gold Nanoparticles for the Fenton Reaction by Light. *J. Am. Chem. Soc.* **2011**, *133* (7), 2218−2226.

(53) Peon, J.; Tan, X.; Hoerner, J. D.; Xia, C.; Luk, Y. F.; Kohler, B. Excited State Dynamics of Methyl Viologen. Ultrafast Photoreduction in Methanol and Fluorescence in Acetonitrile. *J. Phys. Chem. A* **2001**, *105* (24), 5768−5777.

(54) Marimuthu, A.; Zhang, J.; Linic, S. Tuning Selectivity in Propylene Epoxidation by Plasmon Mediated Photo-Switching of Cu Oxidation State. *Science (Washington, DC, U. S.)* **2013**, *339* (March), 1590−1593.

(55) Jawad, A.; Lu, X.; Chen, Z.; Yin, G. Degradation of Chlorophenols by Supported Co−Mg−Al Layered Double Hydrotalcite with Bicarbonate Activated Hydrogen Peroxide. *J. Phys. Chem. A* **2014**, *118* (43), 10028−10035.

(56) Catalán, J.; Díaz, C.; Barrio, L. Analysis of Mixed Solvent Effects on the Properties of Singlet Oxygen (1Δg). *Chem. Phys.* **2004**, *300* (1), 33−39.

(57) Yuan, L.; Shen, J.; Yan, P.; Chen, Z. Interface Mechanisms of Catalytic Ozonation with Amorphous Iron Silicate for Removal of 4-Chloronitrobenzene in Aqueous Solution. *Environ. Sci. Technol.* **2018**, *52* (3), 1429−1434.

(58) Ogino, K.; Kodama, N.; Nakajima, M.; Yamada, A.; Nakamura, H.; Nagase, H.; Sadamitsu, D.; Maekawa, T. Catalase Catalyzes Nitrotyrosine Formation from Sodium Azide and Hydrogen Peroxide. *Free Radical Res.* **2001**, *35* (6), 735−747.

(59) Schuchmann, M. N.; Bothe, E.; von Sonntag, J.; von Sonntag, C. Reaction of OH Radicals with Benzoquinone in Aqueous Solutions. A Pulse Radiolysis Study. *J. Chem. Soc., Perkin Trans. 2* **1998**, *2*, 791−796.

(60) Wang, Y.; Cao, H.; Chen, L.; Chen, C.; Duan, X.; Xie, Y.; et al. Tailored Synthesis of Active Reduced Graphene Oxides from Waste

Graphite: Structural Defects and Pollutant-Dependent Reactive Radicals in Aqueous Organics Decontamination. *Appl. Catal., B* **2018**, *229*, 71−80.

(61) Xia, Q.; Yin, J. J.; Cherng, S. H.; Wamer, W. G.; Boudreau, M.; Howard, P. C.; Fu, P. P. UVA Photoirradiation of Retinyl Palmitate - Formation of Singlet Oxygen and Superoxide, and Their Role in Induction of Lipid Peroxidation. *Toxicol. Lett.* **2006**, *163* (1), 30−43.

(62) Aslam, U.; Rao, V. G.; Chavez, S.; Linic, S. Catalytic Conversion of Solar to Chemical Energy on Plasmonic Metal Nanostructures. *Nat. Catal.* **2018**, *1* (9), 656−665.

(63) Kasprzyk-hordern, B.; Ziółek, M.; Nawrocki, J. Catalytic Ozonation and Methods of Enhancing Molecular Ozone Reactions in Water Treatment. *Appl. Catal., B* **2003**, *46*, 639−669.

(64) Zhang, T.; Li, W.; Croué, J. P. Catalytic Ozonation of Oxalate with a Cerium Supported Palladium Oxide: An Efficient Degradation Not Relying on Hydroxyl Radical Oxidation. *Environ. Sci. Technol.* **2011**, *45*, 9339−9346.

(65) U.S. Environmental Protection Agency. National Primary Drinking Water Regulations; 2001. https://www.epa.gov/sites/production/files/2016-06/documents/npwdr_complete_table.pdf.

(66) Hu, H.; Tian, Z.; Liang, J.; Yang, H.; Dai, A.; An, L.; Wu, H.; Yang, S. Surfactant-Controlled Morphology and Magnetic Property of Manganese Ferrite Nanocrystal Contrast Agent. *Nanotechnology* **2011**, *22* (8), 85707.

(67) Lu, J.; Ma, S.; Sun, J.; Xia, C.; Liu, C.; Wang, Z.; Zhao, X.; Gao, F.; Gong, Q.; Song, B.; et al. Manganese Ferrite Nanoparticle Micellar Nanocomposites as MRI Contrast Agent for Liver Imaging. *Biomaterials* **2009**, *30* (15), 2919−2928.